M. J. Lloyd, A. J. London, M. Gilbert, C. S. Becquart, C. Domain, E. Martinez, M. Moody, P. A. J. Bagot, D. Nguyen-Manh, D.E. J. Armstrong

Interaction of Transmutation Products with Precipitates, Dislocations and Grain Boundaries in Neutron Irradiated W

Interaction of Transmutation Products with Precipitates, Dislocations and Grain Boundaries in Neutron Irradiated W

M. J. Lloyd, A. J. London, M. Gilbert, C. S. Becquart, C. Domain, E. Martinez, M. Moody, P. A. J. Bagot, D. Nguyen-Manh, D.E. J. Armstrong
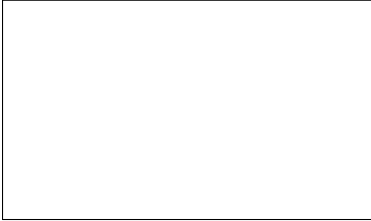
Graphical Abstract

Interaction of Transmutation Products with Precipitates, Dislocations and Grain Boundaries in Neutron Irradiated W

M. J. Lloyd,A. J. London,J. Haley,M. R. Gilbert,C. S. Becquart,C. Domain,E. Martinez,M. Moody,P. A. J. Bagot,D. Nguyen-Manh,D. E. J. Armstrong

Highlights

Interaction of Transmutation Products with Precipitates, Dislocations and Grain Boundaries in Neutron Irradiated W

M. J. Lloyd,A. J. London,J. Haley,M. R. Gilbert,C. S. Becquart,C. Domain,E. Martinez,M. Moody,P. A. J. Bagot,D. Nguyen-Manh,D. E. J. Armstrong

- Research highlights item 1

- Research highlights item 2

- Research highlights item 3

Interaction of Transmutation Products with Precipitates, Dislocations and Grain Boundaries in Neutron Irradiated W

M. J. Lloyd[a,b,*], A. J. London[b], J. Haley[a], M. R. Gilbert[b], C. S. Becquart[e,c], C. Domain[c,d], E. Martinez[f,g], M. Moody[a], P. A. J. Bagot[a], D. Nguyen-Manh[a,b] and D. E. J. Armstrong[a]

[a]*Department of Materials, University of Oxford, Parks Road, Oxford, UK, OX1 3PH*

[b]*Culham Centre for Fusion Energy, United Kingdom Atomic Energy Authority, Culham, Abingdon, Oxfordshire, OX14 3DB, UK*

[c] *Univ. Lille, CNRS, INRAE, Centrale Lille, UMR 8207-UMET-Unité Matériaux et Transformations, F-59000 Lille, France*

[d]*Laboratoire commun EDF-CNRS Etude et Modélisation des Microstructures pour le Vieillissement des, Matériaux (EM2VM), France*

[e]*EDF-R&D, Département Matériaux et Mécanique des Composants (MMC), Les Renardières, F-77818, Moret sur Loing Cedex, France*

[f]*Department of Mechanical Engineering, Clemson University, Clemson, SC 29634, USA*

[g]*Department of Materials Science and Engineering, Clemson University, Clemson, SC 29634, USA*

ARTICLE INFO

ABSTRACT

Tungsten is a primary candidate materials for the high neutron flux, high temperature components of a future demonstrate fusion reactor. Despite this, there is a lack of data on W under fusion relevant neutron doses and irradiation temperatures. Transmutation reactions result in the production of Re and Os solute atoms. In this study, single crystal and polycrystalline W samples irradiated at the High Flux Reactor (HFR) at 900 °C were characterised using Atom Probe Tomography (APT). Bulk chemical and isotopic concentration predictions were validated by analysing the mass spectrum from APT experiments. A post irradiation composition of W-1.263±0.149at.%Re-0.083±0.017at.%Os-0.009±0.004at.%Ta was measured in the single crystal sample, whereas W-1.090±0.067at.%Re-0.080±0.016at.%Os-0.009±0.004at.%Ta was measured for the polycrystalline. APT showed that a high number density of Re and Os rich precipitates had formed due to neutron irradiation. These typically presented with a core rich in Re and Os, surrounded by a less dense Re rich cloud. Multiple analysis methods were applied to investigate the composition of these clusters. APT showed that in the centres of some of the precipitates, a dense rod-shaped Re and Os rich region was correlated with these higher compositional measurements obtained using line profile analysis. Line profile analysis suggests that in the centre of the precipitates, the threshold composition for σ phase formation may have been reached, as has been observed on a larger scale in higher transmutation rate experiments. Line dislocations and dislocation loops were observed to be decorated with both Re and Os, in agreement with predictions from DFT.

1. Introduction

Understanding the interaction between neutron induced transmutation products and microstructural features including dislocations and grain boundaries is vital for the development of reliable components for use in a demonstration fusion power station (DEMO) and future power stations. Transmutation of elements in reactor components leads to the production of light elements such as H and He, as well as other elements adjacent the parent in the periodic table, through a sequence of neutron reactions and subsequent nuclide decays. For materials such as tungsten, which has a relatively high cross section for neutron absorption reactions [1, 2], transmutation to adjacent elements is significant [3, 4], and results in components which have a time dependant composition [3]. Transmutation reactions are also most significant in the high neutron flux regions of the reactor, such as in the first wall (FW) and divertor regions which together make up the plasma facing components (PFCs). It is in these regions that the deployment of tungsten components is envisaged.

W has a number of attractive properties which make it the primary candidate for use in the PFCs, including a comparatively low induced long-term activity after neutron irradiation (in pure form [5]), a high melting temperature (3695K [6]), good thermal conductivity ($165 \mathrm{Wm}^{-1}\mathrm{K}^{-1}$ at room temperature [7]) and high resistance to sputtering under H/He plasma exposure [8]. Tungsten is not a commonly used engineering material within the nuclear industry because of its inherently poor mechanical properties (DBTT≈623-723 K [9, 10] and brittle behaviour at room temperature [11]), its tendency to undergo inter-granular fracture [12, 13], and due to difficulties in its forming. Furthermore, neutron irradiation of W has been linked to a significant degradation in thermal and mechanical properties. A shift in the DBTT of between 500 and 1000K has been observed in neutron irradiated tungsten from the HFR and BR2 reactors [9, 14]. Both nanoindentation and microindentation have been also used to measure irradiation induced hardening in ion implanted samples [15–20], and in neutron irradiated samples from various fission spectrum reactors [21–25]. The thermal diffusivity of W is another important consideration for the PFCs, and various studies have measured significant decreased following neutron [23] and ion irradiation [26, 27]. The production of solute elements through transmutation, and subsequent radiation-induced precipitation, is one of the key contributors to this property degradation under neutron

✉ matthew.lloyd@materials.ox.ac.uk (M.J. Lloyd);
david.armstrong@materials.ox.ac.uk (D.E.J. Armstrong)
ORCID(s): 0000-0003-4479-5469 (M.J. Lloyd)

irradiation, along with the formation of dislocation loops and voids [21].

In W, transmutation leads to the production of Re and Os, by a sequence of (n,γ) neutron absorption reactions and β^- decays. Ta is also produced primarily via the β^+ decay of isotopes which have undergone (n,2n) neutron loss reactions [28], but is not thought to have a major impact on mechanical properties [17]. The amount of transmutation is strongly dependant on the incident neutron energy spectrum, with lower energy neutrons having a higher cross section for absorption. This makes comparison between samples irradiated at different reactors very difficult, as there are major differences in the neutron energy spectrum caused by the design of the reactor, the presence of adjacent samples and the physical location within the reactor core. However, on average, reactors with a higher proportion of thermal neutrons generate samples with transmutation levels significantly greater than is expected for a DEMO reactor, per dpa of damage. Reactors with a high proportion of fast neutrons, or experiments in which the thermal neutron population has been decreased through canister design, generate a smaller quantity of transmutation products per dpa of damage [22, 29], but still significantly higher than is expected for a DEMO reactor [3]. Even at DEMO transmutation levels, the W components the reactor are expected to generate a significant quantity of Re and Os during their lifetime [4, 28, 30, 31].

Alloying W with Re (up to a maximum of around 8at.%Re) is known to reduce the DBTT [12, 32–35] and results in a decrease in hardness [32]. However, increasing the Re content further results in an increase in hardness which is associated with the formation of the brittle, intermetallic σ-phase (WRe) [32]. Under irradiation the benefits of Re alloying are reversed, due to radiation induced segregation of Re. Studies between the 1960s and 1980s were performed on neutron irradiated W-Re alloys, as this system was investigated for use in high temperature thermocouples for nuclear applications [32–35]. Subsequent studies began to focus more on the irradiation of pure W samples, as its application within the PFCs of a fusion reactor was explored. Neutron irradiation of pure W samples at the EBR-II reactor led to the observation of the Re rich χ phase (WRe$_3$), rather than the expected σ phase [36]. Several subsequent studies have also observed this phenomena, with a number reporting a mixture of σ or χ phase. TEM and STEM analysis of these precipitates generally find a needle or rod shaped morphology. Microstructural characterisation of samples from various reactors have found a combination of dislocation loops, voids and Re rich precipitates, the ratio of which depends on the irradiation temperature and dose. At higher doses where Re and Os production is significant, the hardening response is primarily caused by Re rich precipitates [21].

APT analysis of samples irradiated in experiments with comparatively low transmutation rates found Re rich clusters, rather than precipitates consistent with either σ or χ phase. APT analysis of samples from HFIR with higher levels of transmutation have found needle shaped precipitates that have contain approximately 20at.%Re and 13at.%Os [37].

STEM-EDX analyses performed on samples irradiated at the BR2 reactor, producing relatively low transmutation rates, found clear evidence for both σ and χ phase, including evidence for an Os rich, intermetallic χ phase (WOS$_3$), which is not present in the binary W-Os phase diagram [38–40].

Ion irradiation does not induce transmutation reactions, and has been carried out in pure-W, W-Re, W-Re-Ta and W-Re-Os alloys [15–17, 20]. In general Re clustering has been consistently observed using APT, but not the formation of phases with a composition consistent with either the σ or χ phase.

Computational studies suggest that kinetic transport of Re, via mixed-interstitial dumbbell mediated migration is responsible for the observed precipitation of Re, well below the expected solubility limit [41, 42]. However, these studies focus on binary W-Re, and do not fully account for void formation. The impact of Os on the microstructure is less clear, but DFT modelling suggests that Os may play a more significant role than Re, due to its stronger binding with point defects. Os was also found to decorate dislocations in APT of unirradiated W-Os in 1983 by Eaton and Norden [43]. Xu et. al observed that Os had a strong impact on the cluster structure, with the addition of 1at.%Os acting to suppress Re clustering, by preferentially forming small Os rich clusters [16]. Higher temperature ion irradiation by Lloyd et. al confirmed that this effect was significant, even at lower doses and lower nominal Os concentrations, as low as 0.1at.%Os [44, 45].

In this study, a characterisation of the post-irradiation microstructure of high temperature, low transmutation rate, neutron irradiated single crystal and polycrystalline W is presented. In this study, we use APT to focus on the composition of the observed precipitates and investigate whether some of the precipitates are consistent with σ or χ phase formation. We also investigate the decoration of dislocation loops and grain boundaries within the irradiated material and compare the microstructure between single crystal and polycrystalline W. DFT simulations were also performed for W-Re and W-Os to provide insight into the experimental findings.

2. Methodology

2.1. Samples and Neutron Irradiation

The samples used in this study were irradiated between 2008 and 2009 as part of the ExtreMat-II programme at the High Flux Reactor (HFR) in Petten, Netherlands. Samples of commercially pure single crystal and polycrystalline W were purchased from Metal Crystals and Oxides Limited, Cambridge UK (no longer trading). The samples were 100mm long rods, 10mm in diameter. The polycrystalline sample had a fine grained microstructure dominated by elongated grains oriented along the rolling direction. Previous analysis of these samples showed that there was an average grain size of 100x10um with sub grains approximately 20x2um [46]. The samples were polished using a series of successively finer SiC grit papers, diamond suspension paste di-
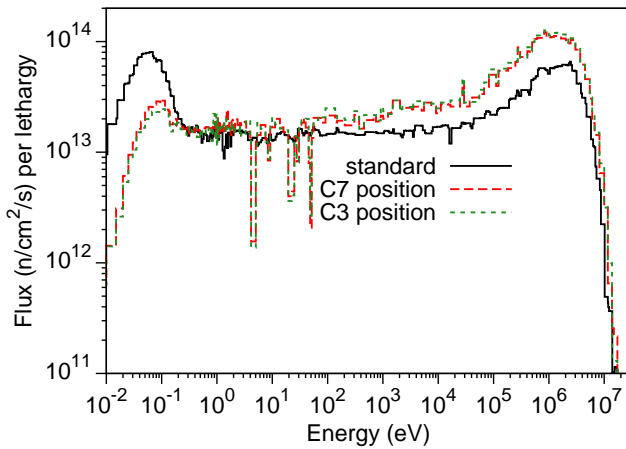
Figure 1: Local neutron energy spectrum received by samples in the two reactor locations in HFR (C7 and C3), overlaid over the averaged neutron energy spectrum for the reactor.

luted with water (6um, 3um and 1um) and finally using colloidal silica. The samples were then annealed at 1673K for 24 hours.

The samples underwent neutron irradiation at HFR, starting in 2008. Technical problems resulted in neutron irradiation being stopped in the summer of 2008, and resumed in the spring of 2009. Irradiation ended in April 2009. The samples were loaded alongside others into the HFR reactor and received a 208 full power day irradiation in 2 locations at 1173K. The samples were located in positions C7 and C3 in drums 3 and 4. In total the samples received a neutron fluence of 1.21×10^{26} m^{-2} (6.5×10^{25} m^{-2} at an energy above 1×10^{-1} MeV): 6.8×10^{18} m^{-2} s^{-1} in the first location and 6.6×10^{18} m^{-2} s^{-1} in the second location. The presence of an adjacent, strong thermal neutron absorber caused local modification of the neutron energy spectrum, reducing the thermal neutron population, as shown in figure 1. Following irradiation the samples had a specific activity of 8.2 MBqkg^{-1} after 5 years of cooling.

The dose in dpa received by the sample and the transmutation level were quantified via nuclear inventory modelling using FISPACT-II [47], in simulations carried out using a displacement threshold energy of 55 eV. The simulations used the TENDL-2015 [48] nuclear cross section data library and accounted for self-shielding effects in the material using appropriate probability tables (see [28] for details), and also included the impact of the two different locations (C7 and C3) within the reactor via appropriate use of the local energy spectrum (figure 1). The simulations were performed for the 208 days of exposure and 6 years of decay following removal from the reactor [29, 49].

A total dose of 1.67 dpa and a post-irradiation composition of 1.4at.%Re - 0.1at.%Os - 0.02 at.%Ta was predicted. This composition was confirmed by Abernethy et. al using γ–ray spectroscopy of the ^{186}Re decay and SEM-EDX measurements [9, 46, 49], and by Lloyd et. al using APT [29]. Both EDX and APT of the single crystal sample showed good agreement with the FISPACT-II modelling (see table 1).

2.2. Post-Irradiation Sample Preparation

APT relies on the fabrication of sharp needle shaped samples in order to maximise the evaporation field at the tip. In this research, a Focused Ion Beam (FIB) liftout technique was used to prepare site specific and bulk samples. FIB work was carried out remotely in hot cell facilities at the Materials Research Facility (MRF), United Kingdom Atomic Energy Authority, using an FEI Helios dual beam FIB-SEM system. The calculated activity from an individual lift-out was >1Bq which allowed for non-active APT/TEM analysis in facilities at the David Cockayne Centre for Electron Microscopy (DC-CEM), and Research Group in Atom Probe Tomography at Oxford Department of Materials.

The cantilever was removed from the sample surface using an Omniprobe micromanipulator and cross sections were mounted onto silicon posts on a 22 grid coupon, using Pt deposition. An initial electron beam deposited Pt layer was used to protect the sample surface during subsequent ion beam Pt deposition. The samples were sharpened into needles using a series of successively smaller annular milling patterns and lower beam currents (1.5 nA - 4.0×10^1 pA) and an acceleration voltage of 3.0×10^1 kV. At a tip diameter of approximately 50-1.00×10^2 nm in diameter, a final polishing stage using an acceleration voltage of 2 kV and a beam current of 3.00×10^2 pA was used to remove approximately 5.00×10^2 nm of Ga implanted material from the top of the needle.

Targeted APT was performed on grain boundaries of the polycrystalline sample, using a site-specific FIB lift-out procedure. The boundary of a grain was chosen (the size of which indicated that it was a sub-grain boundary) and a protective layer of Pt was deposited using the procedure outlined above. The grain boundary was positioned centrally within the needle during sharpening, using the contrast between adjacent grains in the electron and ion images. The GB was positioned so that it was within the top 1.00×10^2-3.00×10^2 nm of the tip. When GB was within approximately 5.00×10^2 nm of the apex, a 2 kV polishing stage was applied until the distance between the GB and the apex of the tip was removed from the sample.

2.3. Atom Probe Tomography

APT was carried out in a CAMECA LEAP 5000 XR at the University of Oxford in laser-assisted mode, using a sample temperature of 55K, a laser pulse energy of 80-125pJ and a pulse frequency of 100-200kHz. A medium sensitivity fast emission control (FEC) setting, with a voltage step of 5% was used in order to mitigate against sudden increases in ion evaporation observed during the evaporation of a Re rich area. Parameters were chosen primarily to increase the yield of data from each specimen, as a high sample fracture rate occurred in both single crystal and polycrystalline samples.

In total, 10 samples were obtained from the single crystal sample giving a total count of 2.141×10^7 ranged ions. For the polycrystalline sample, 2 samples containing a section of a grain boundary were obtained, and 4 without grain boundaries, with a total count of 1.371×10^7 ions. The data was

Table 1
Bulk sample solute concentration from transmutation measured using APT. Uncertainty quantified using under and over ranging approach. Compared to FISPACT-II results [29] and EDX measurements [9].

Sample	Re (at.%)	Os (at.%)	Ta (at.%)
Single Crystal	1.263±0.149	0.083±0.017	0.009±0.004
Polycrystalline	1.090±0.067	0.080±0.016	0.009±0.004
FISPACT-II	1.4	0.1	0.02
EDX [9]	1.2	0.1	Undetectable

reconstructed and visualised using IVAS 3.8.2, using a under/over peak ranging method described in previous publications [29]. Reconstructions were carried out using a tip radius estimated by the voltage curve in IVAS as an input, unless specified otherwise. The mass spectra of multiple APT data sets were analysed using the CompositionFromPosList.m Matlab script in the AtomProbeLab software package [50].

2.4. Density Functional Theory Calculations

The density functional theory (DFT) calculations were done within the projector augmented wave (PAW) method as implemented in the Vienna ab initio simulation package VASP [51, 52]. The exchange-correlation functional is described by the generalized gradient approximation (GGA) of PBE [53]. For the self interstitial atom (SIA) loop calculations, 1458 bcc positions supercells were used with Gamma point representation of the Brillouin zone (referred to as 1 kpt calculations). A selected number of configurations were also calculated using 2 x 2 x 2 kpoints. All atomic relaxations were performed under constant volume condition. A perfect $1/2 \langle 111 \rangle$ loop containing 37 SIA has been introduced in the middle of the supercell and the binding energy of different solute atoms determined for various positions of the solute. The influence of the pressure due to the use of constant volumes has been evaluated using the method proposed by Varvenne et al.[54] to take into account long range interactions. Once point defect energies have been calculated using VASP, they are corrected by subtracting artificial interaction energy arising from periodic boundary conditions. The calculations were done using the minimal set regular PAW which considers s and d electrons as valence electrons. We estimated the error for not taking into account the semi-core states and only 1 kpt to be around 0.1 eV, the uncertainty being always the highest for Os and Ta.

3. Results

3.1. Mass Spectrum Analysis

As discussed in the previous section, the post-irradiation composition of the samples was predicted using FISPACT-II nuclear inventory modelling. To provide a thorough validation of these calculations, analysis of the APT mass spectrum was performed to measure the chemical composition

and isotopic abundance. Previously published studies have applied this technique to a small sample volume [29]. In total, 6 samples were obtained from the single crystal sample giving a total ion count of 1.626×10^7 ranged ions. For the polycrystalline sample, 2 samples containing a section of the grain boundary were obtained, and 4 without grain boundaries, with a total ion count of 1.371×10^7 ions.

Mass peak identification in APT data relies on manual operator input to define the corresponding element and peak ranging width, and is therefore an important source of uncertainty in the overall sample composition. To quantify this uncertainty, two approaches of ranging the mass peaks are applied: one which is defined from background-to-background and another which only accounts for the central part of each mass peak, as outlined in [29]. This process was applied to all of the data sets obtained and averaged to give a bulk composition. The reported value for bulk composition of solute component, x, in this study is therefore given by:

$$x = \frac{1}{N} \sum_{i}^{N} x_i \pm \frac{|x_{over}^i - x_{under}^i|}{2} \qquad (1)$$

where x_{over}^i and x_{under}^i refer to the measured composition using the two ranging approaches outlined above, and N is the total number of APT data sets used for analysis. The standard approach to separating the contributions to an individual mass peak, and correctly labelling the overlapping peaks with the corresponding elements in APT data, is to use the heights of the adjacent non-overlapping mass-to-charge-state peaks to determine the ratio of the elements in the peak. In samples in which transmutation has not occurred, this is possible because the heights of the individual isotopic peaks for an element are distributed according to the natural abundance for that element. In the case of the samples discussed here this approach cannot be used because the Re and Os are introduced "artificially" via neutron reactions with isotopes of W. The predicted distribution of isotopes from FISPACT-II calculations indicate that overlap in mass-to-charge-state peaks corresponding to isotopes of W, Re and Os with equivalent atomic mass number is, in fact, minimal, and allowed peak ranging without deconvolution. This is in contrast to situation in [37], where higher transmutation levels in those experiments meant that deconvolution was required. The minimal overlap is due to the relatively short half-lives of the isotopes in question [3]. There is no overlap between W isotopes as the ^{185}W and ^{187}W isotopes have half-lives of 75.1 days and 23.72 hours respectively [3]. Both of these isotopes are produced, during and affect irradiation, via transmutation reactions, but do not overlap with the ^{185}Re and ^{187}Re mass-to-charge-state peaks because they decay quickly. Because the time between removal from the reactor and APT analysis is several years, the contribution to the ^{185}Re and ^{187}Re mass-to-charge-state peaks is minimal and no further peak deconvolution needs to be applied.

The averaged bulk compositions from the single and polycrystalline samples are summarised in table 1, alongside the predictions from FISPACT-II and EDX measurements carried out elsewhere [9]. Overall the measured composition

W Re

40nm
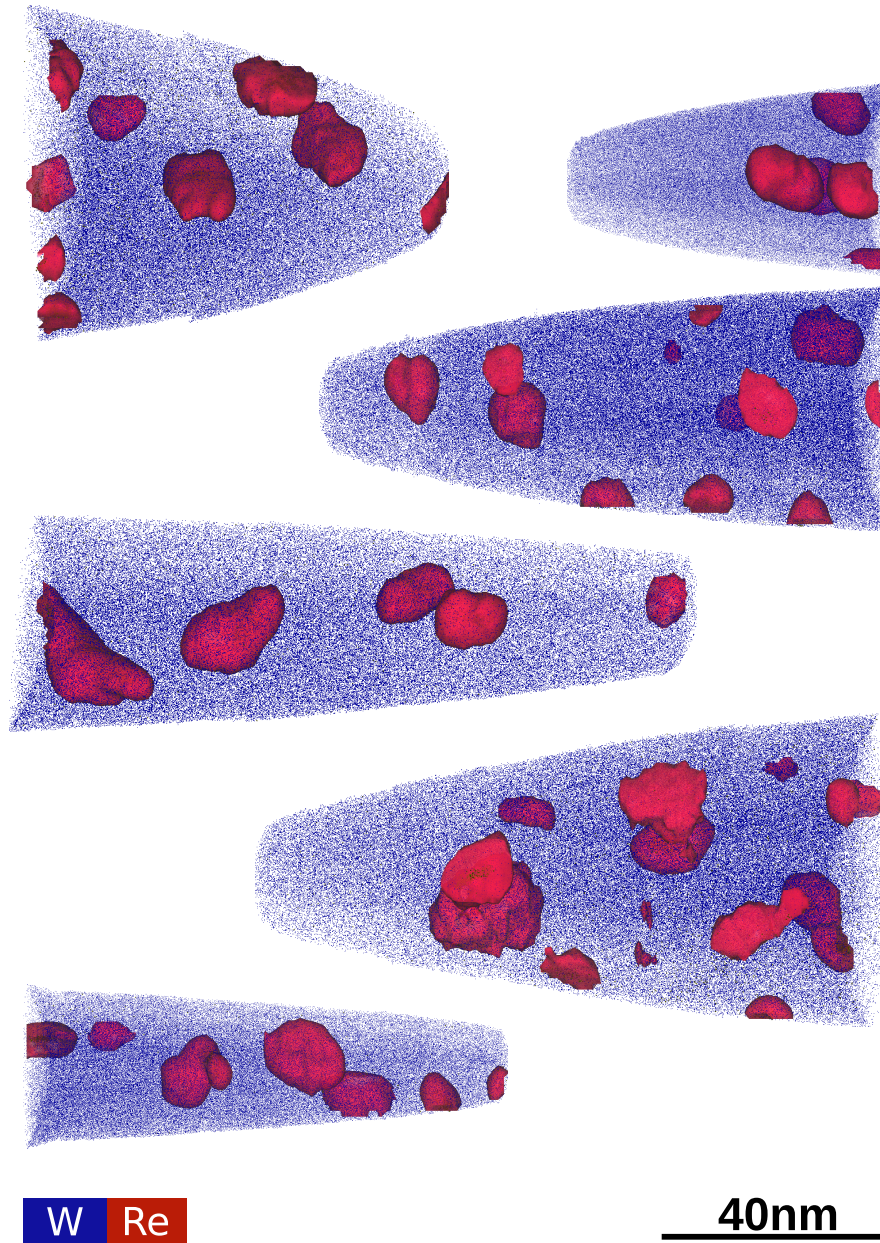
Figure 2: APT Reconstruction of samples taken from single crystal neutron irradiated sample, showing ≈5-20% of the detected W atoms in blue, 100at.% of the detected Os atoms in green, and with 5at.%Re isoconcentration surfaces shown in red to highlight the location of the clusters.

compares well to both EDX and FISPACT-II, with only a slight overestimation in the Re content detected. The single crystal samples have a higher overall composition than the polycrystalline samples, which is likely due to the proximity of these APT samples to grain boundaries, which have been shown to be decorated with Re and Os. This highlights the site specific nature of APT and represents a source of uncertainty which is not quantified here. Overall however, the bulk measurements support the use of FISPACT-II calculations for assessing post-irradiation sample compositions. APT measurements were also in close agreement with EDX

carried out by Abernethy et. al [9].

The distribution of isotopic abundances was analysed further by creating a range file in which individual isotopes were identified as independent custom defined elements. This file describes the location and width of the region in the mass-to-charge data for which counts are associated with a particular ionic species. The same approach to under and over ranging peaks in the mass spectrum data described previously was used to evaluate the uncertainties such that the composition of an isotope is given by equation 1. Table 2 shows the isotopic abundances predicted by FISPACT-II modelling

Re Os   40nm
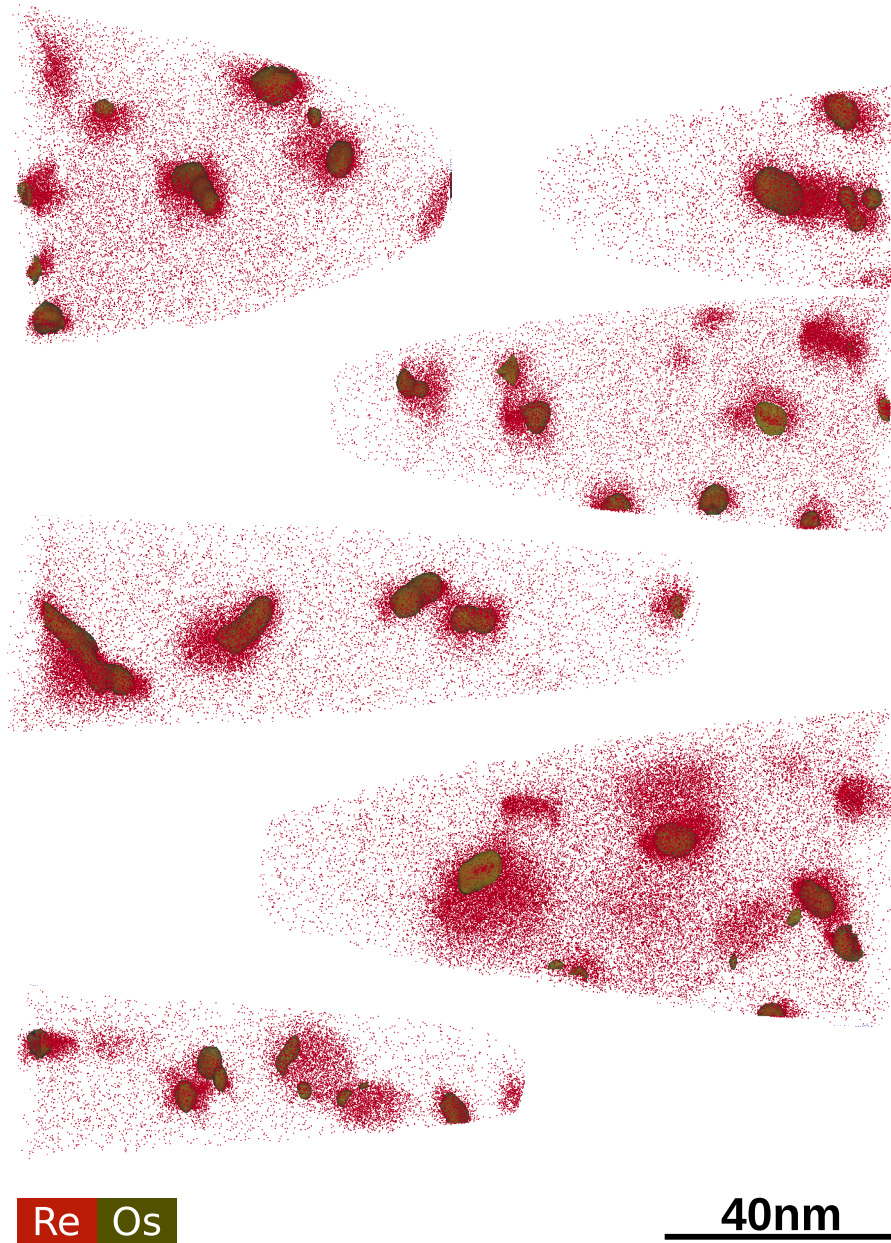
Figure 3: APT Reconstruction of samples taken from single crystal neutron irradiated sample. Equivalent data to that shown in figure 2, however, for visual clarity, only Re atoms (red spheres, 0.1nm in diameter) are shown, together with Os isoconcentration surfaces at 1.5at.%.

as well as the measured abundances in the single and poly-crystalline samples from APT (a further 60+ isotopes were predicted by FISPACT in lower concentrations).

The modelling predicts that mass-to-charge-state overlaps for the irradiation conditions experienced by this sample were minimal due to the short half-lives of the other isotopes formed under irradiation. FISPACT-II predicts that ^{187}Os should account for only 0.01% of the 187 mass peak, with the rest of the counts coming from ^{187}Re and zero contribution from ^{187}W. Again with the 185 peak, minimal overlap is predicted with only 3.54×10^{-6} % predicted to arise

from isotopes other than ^{185}Re. There is slight deviation between the predicted and measured ^{187}Re signal, that could indicate slight inaccuracies in the nuclear data, variation in the local neutron spectrum or because of artefacts in APT. Table 2 demonstrates clearly that given an accurate description of the neutron energy spectrum, FISPACT-II simulations can be used to give a reliable prediction of the post-irradiation composition in W and, in this case, is a reliable method for quantifying transmutation effects. It also provides confidence that the mass peak ranging approach used in this study is valid, and that further spatial analysis can be

Table 2

Comparison between the calculated distribution of isotopes and the measured distribution from APT produced by transmutation from 208 day neutron irradiation at HFR and 6 years of cooling, as a percentage of the total number of atoms in the simulation and the total number of ranged ions in APT. The 11 most commonly occurring isotopes from the simulation are included, isotopes with lower concentration could not be separated from background using APT. Uncertainty on the concentration from APT is estimated by comparing different ranging approaches, background-to-background and at FWHM.

Isotope	FISPACT-II (at.%)	Single Crystal (at.%)	Poly-crystalline Bulk (at.%)
^{184}W	30.97	31.9 ± 0.9	31.9 ± 1.1
^{186}W	26.99	26.1 ± 0.8	26.6 ± 0.3
^{182}W	25.35	24.8 ± 0.6	24.1 ± 1.3
^{183}W	15.02	15.4 ± 0.6	15.0 ± 0.5
^{187}Re	1.34	1.24 ± 0.06	1.03 ± 0.05
^{188}Os	0.10	0.08 ± 0.02	0.08 ± 0.03
^{180}W	0.10	0.11 ± 0.01	0.08 ± 0.01
^{185}Re	0.09	0.11 ± 0.01	0.11 ± 0.01
^{181}Ta	0.02	0.01 ± 0.01	0.01 ± 0.01
^{186}Os	0.01	Undetectable	Undetectable
^{189}Os	0.002	Undetectable	Undetectable

performed on this material.

3.2. Transmutation Product Precipitation

As reported previously, precipitation of Re and Os was observed in both single and polycrystalline samples. As demonstrated in figures 2-5, both the precipitation of Re and Os, as well as the core shell Os structure observed previously has been formed in both single and polycrystalline samples. In this section an overview of the observed clusters is given before further analysis in section 3.3. Overall a greater volume of material was obtained for the single crystal sample because the polycrystalline material produced a significantly lower ion yield in the APT experiment, prior to fracture of the specimen.

3.2.1. Single Crystal

Large clusters of Re and Os (relative to the reconstruction) were observed in all of the 6 single crystal samples analysed. Figure 2 shows reconstructions of 6 successful APT needles taken from the single crystal sample, with between 5 and 20 at.% of the detected W atoms in blue shown for visual clarity, and 100at.% of detected Os atoms in green, and with 5at.%Re isoconcentration surfaces shown in red to highlight the location of the clusters. Ta was present in very small concentrations and was not shown to be correlated with the clusters and therefore is not shown in figure 2. As is shown in figures 2 and 3, strong segregation of both Re and Os has occurred. Os isoconcentration surfaces show that precipitation of Os has occurred, despite the much lower nominal concentration (≈ 0.08at.%Os). The majority of the clusters shown in figure 2 exhibited this core shell structure of Os, surrounded by Re, as highlighted in previous studies [29]. Higher than usual atomic density associated with some of the precipitates indicates that some of the precipitates could be attached to voids or in fact be voids decorated

with Re and Os, however, further correlative analysis is required to confirm or disprove this hypothesis.

3.2.2. Polycrystalline

Reconstruction of the APT needles taken from the polycrystalline samples show a similar microstructure to the single crystal sample. Figure 4 shows the reconstructed samples with between 5 and 20 at.% of the detected W atoms in blue shows for visual clarity, and 100at.% of Os atoms in green, and with 5at.%Re isoconcentration surfaces shown in red to highlight the location of the clusters. As was observed for the single crystal sample in figures 2 and 3, large clusters of Re are observed which typically contain a core rich in both Re and Os. Strong Os precipitation is observed, despite the low nominal Os concentration in the sample of 0.08at.%. As shown in figures 2 and 4, some of the precipitates are elongated in one direction. These rod shaped precipitates are consistent with the shapes observed in higher transmutation level samples from HFIR [55]. Some elongation or rod shaped cluster formation is also visible in figure 3 for the single crystal material.

Previous analysis of the material discussed in this paper found clear evidence for the presence of radiation induced voids [29, 49], EDX analysis of which showed decoration with Re and Os. Atomic density artefacts associated with Re and Os clusters suggested that some of these features within the APT reconstruction were in fact associated with voids. Trajectory focusing aberrations of the ions emitted from the periphery of the void leads to regions of higher than expected atomic density in the reconstructed APT data [56, 57]. However, the effect of these features on the reconstructed data is strongly dependant on the materials system being studied, the size of the void and the chemical nature of any segregation effects. Furthermore, precipitates with a low field evaporation threshold are expected to result in an increase in the
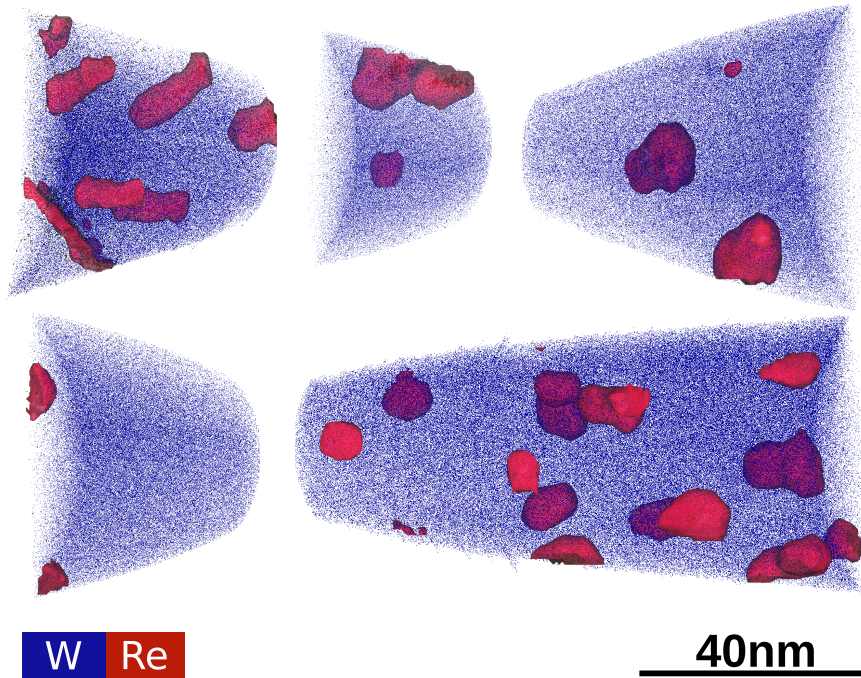
Figure 4: APT Reconstruction of samples taken from polycrystalline neutron irradiated sample, showing ≈1% of the detected W atoms in blue for visual clarity and red isoconcentration surfaces at 5at.%Re.

local atomic density during reconstruction, thus it is generally not possible to unambiguously distinguish decorated voids and these precipitates in the reconstruction based on associated atomic density artefacts alone.

High angle annular dark field (HAADF) imaging of the samples measured a cavity number density of 2.4×10^{22} m^{-3} for the polycrystalline material and 2.8×10^{21} m^{-3} for the single crystal. Previous TEM measurements found cavity number densities of 4.0×10^{21} for the polycrystalline and 2.5×10^{21} for the single crystal material [49]. By comparison, in the reconstructed APT data the number density of Re and Os rich precipitates was measured to be 1.5×10^{23} m^{-3} and 9.65×10^{22} m^{-3} for the polycrystalline and single crystal material respectively. The higher number density of Re and Os rich features in the APT data suggests that not all of the clusters are associated with voids, and a number of clusters are present which are either isolated, or attached to voids too small to be resolved using STEM. This combined analysis shows that care must be taken when applying the method for analysing voids in APT data suggested by Wang et. al, particularly in materials which contain precipitates with a lower field evaporation threshold than the surrounding matrix.

As shown in table 1, a small quantity of Ta was produced in the samples under irradiation. Analysis of the APT data shown in figures 2–5 clearly showed that Ta had not segregated to the clusters, and no measurable enrichment of Ta was found within either the clusters, or at other microstructural features such as grain boundaries or dislocations.

3.3. Cluster Composition Analysis from APT
3.3.1. Maximum Separation Algorithm

Analysis of the composition of the clusters shown in figures 2-5 was first performed using a conventional Maximum Separation Method (MSM) in which an atom is defined to be within in a cluster if the distance between two solute atoms is within a pre-defined separation distance, d_{max}. This is based on the notion that two nearest neighbour solute atoms are more closely seperated within a cluster than if they were to occur in the W matrix. Discrete clusters are defined by creating networks of mutually clustered solute atoms. Additional parameters used for the analysis include the minimum number of ions in a cluster, N_{min}, an envelope distance, L, and an erosion distance, d_e. For further details on the definitions of these parameters the reader is referred to [58]. A maximum separation distance $d_{max} = 1$ nm , an envelope parameter, $L = 0.7$ nm, an erosion distance of $d_e = 0.25$ nm and a minimum cluster size of $N_{min} = 20$ ions was used, assuming a cluster core comprised of Re and Os atoms and a matrix of W. Practically, this method was implemented within the Posgen program, which is available within the APTTools software package [59].

The average cluster composition for the single and polycrystalline samples are summarised in table 3, with results from experiments at JOYO and HFIR [37, 60, 61]. The samples have a similar average cluster composition (8.6Re-0.6Os for the single crystal and 6.9Re-0.6Os for the polycrystalline) to the pure-W samples irradiated at JOYO (7.6Re-0.2Os), which have a similar transmutation rate to the HFR experiment described here. The HFIR reactor has a considerably higher transmutation rate which produces a higher nominal

Re Os   **40nm**
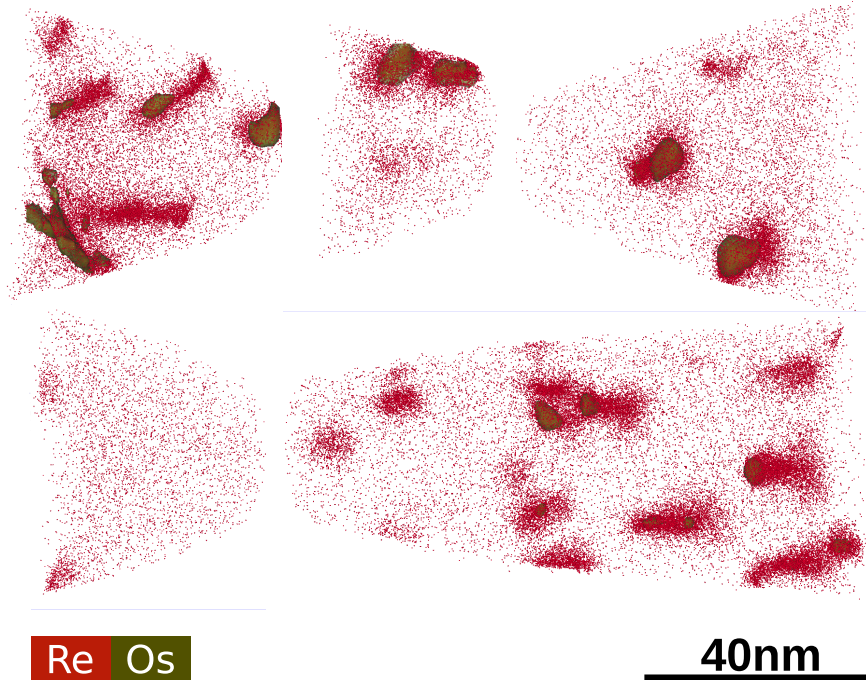
Figure 5: APT Reconstruction of samples taken from the polycrystalline neutron irradiated sample. Equivalent data to that shown in figure 5, however, for visual clarity, only Re atoms (red spheres, 0.1nm in diameter) are shown, together with Os isoconcentration surfaces at 1.5at.%.

post-irradiation Re and Os concentration. The clusters measured in the HFIR sample are on average higher in Re and Os, which can be attributed to the higher transmutation level in that reactor.

The standard deviation of the cluster Re and Os concentrations, σ_{Re} and σ_{Os}, respectively are also given in table 3. The large standard deviation with respect to the mean value indicates that there is a high degree of spread in the individual cluster compositions with respect to the average. This can be seen in figure 7, where each of the black points represents a cluster defined using the MSM. The cluster compositions vary within a range of $\approx$2-20at.%Re, with Os varying between 0 and 5at.%.

The composition of the clusters measured using MSM is not consistent with the formation of σ (black region in figure 7) or χ phase. Similar measurements of materials from experiments in reactors with low transmutation rates such as Joyo have also reported similar average compositions using MSM, that do not correspond to the formation of σ phase [60, 61]. It is worth noting however that the cluster composition is highly sensitive to the cluster search parameters. APT analysis by Edmonson et. al [37] using an isoconcentration surface method has shown a higher average cluster composition, but the bulk sample composition post-irradiation in these samples was higher (W-6.38Re-3.23Os after 1.8dpa compared to W-1.2Re-0.1Os after 1.67dpa in the samples considered in this study). Table 3 also shows the average cluster compositions measured in the single crystal sample using similar Re/Os isoconcentration surfaces. As with the MSM method, the composition measured using a isocon-

centration surface depends on how this boundary is defined, and at what composition, as shown in table 3. Using the 12at.%Re and Os isosurface, a similar Re concentration is seen in clusters in both the HFR and HFIR samples, however the Os concentration is considerably lower for HFR.

Figure 6 (a) and (b) shows a close-up image of a volume extracted from one of the APT data sets shown in figures 2 and 3. The volume was extracted using a Re isoconcentration surface at 5at.%Re, and all of the W atoms are removed for visual clarity. The positions of the Re and Os atoms are plotted separately in red and green respectively. As was observed in several of the clusters shown in figures 2–5, the cluster shown in figure 6 (a) and (b) has a central rod shaped region surrounded by a cloud of Re. Re-isoconcentration surfaces at 25at.%Re suggest that in this central rod shaped region, the composition is higher than 25at.%Re. To investigate the internal structure of the clusters further, a line profile analysis technique was also applied, as is discussed in the following section.

3.3.2. Line Profile Analysis

Figure 6 (a) and (b) show an example of the distribution of Re and Os atoms within a cluster observed in the neutron irradiated W samples, shown in figures 2-5. Analysis of the clusters using MSMs gave a range of compositions consistent with the bcc solid solution region of the ternary phase diagram, shown as the black points in figure 7. The shape of the cluster, and the central Os and Re rich region shown in figure 6 (a) and (b) indicates that although the average cluster composition measured using a MSM is within the solid

Table 3

Average cluster composition in the single crystal and polycrystalline neutron irradiated samples, measured using various methods. The average composition measured in the sample from JOYO and HFIR were also calculated on APT data using a maximum separation algorithm, details of which are given in [60]. The samples irradiated at JOYO and HFIR are polycrystalline pure-W and pre-alloyed W-10at.%Re [61]. The standard deviation of the clusters around the average concentration, σ_x, for the concentration of x is also given, unless marked by a † symbol in which case the value represents the standard error on the mean calculated using $\sigma/\sqrt{N}$, where N is the sample size.

Reactor	Sample	dpa	Analysis Method	Re (at.%)	σ_{Re}	Os (at.%)	σ_{Os}
	Pure-W (Single Crystal)	1.67	Maximum Separation	8.6	3.4	0.6	0.6
	Pure-W (Polycrystalline)	1.67	Maximum Separation	6.9	3.6	0.6	0.5
	Pure-W (Single Crystal)	1.67	Line Profile	24.6	12.4	3.4	2.9
HFR	Pure-W (Polycrystalline)	1.67	Line Profile	19.5	6.7	1.8	1.4
	Pure-W (Single Crystal)	1.67	Isoconcentration (1.5at.%Re-Os)	8.80	4.81	0.61	0.66
	Pure-W (Single Crystal)	1.67	Isoconcentration (12at.%Re-Os)	21.13	3.90	2.33	0.56
	Pure-W (Single Crystal)	1.67	Isoconcentration (25at.%Re-Os)	31.66	4.98	6.61	1.60
Joyo	Pure-W [60]	0.96	Maximum Separation	7.6	-	0.2	-
	W-10Re [60]	0.96	Maximum Separation	20.9	-	3.0	-
	Pure-W [60]	0.90	Maximum Separation	13.4	-	2.6	-
HFIR	W-10Re [60]	0.90	Maximum Separation	16.6	-	7.7	-
	Pure-W [37]	0.10	Isoconcentration (1at.%Re-Os)	11.25	0.83†	0.70	0.08†
	Pure-W [37]	1.80	Isoconcentration (12at.%Re-Os)	19.62	0.41†	13.03	0.46†

solution region, at the centres of the clusters the composition may be significantly higher. To illustrate this, figure 6 shows a line profile analysis of the cluster shown in figure 6 (a) and (b). The cluster core was first identified using a 25at.%Re isoconcentration surface. A cylindrical ROI was defined with a radius of 1.64 nm and a length of 15nm. This ROI was centred on the 25at.%Re isoconcentration surface and manually orientated with the rod shown by the Os atoms in figure 6 (a) and (b).

The concentration along the z-axis of this ROI was split into bins of width 0.1 nm and exported. The data was subsequently rebinned into 20 bins, for which the mean Re and Os concentration, and the standard deviation about the mean was calculated. For each of the points within the bin, the counting errors exported from IVAS were averaged to give the mean counting error for each of the new bins.

Figure 6 shows that despite the measured composition for this cluster using the MSM (<20at.%Re), the Re concentration in the centre of the cluster plateaus at approximately 50at.%Re. Over the equivalent region, the Os concentration also reaches a plateau at around 7at.%Os. The composition taken at the plateau region of this cluster would place it within the σ phase region of the diagram shown in figure 7, despite MSM giving a composition within the bcc solid solution region.

To characterise the cluster cores statistically, an automated approach to performing line profile analyses on all of the clusters shown in figures 2-5 was performed. This process is outlined in the following section.

3.3.3. Automated Line Profile Analysis

An automated method for performing line profile measurements was thus used to sample all of the clusters within the full range of data sets. A MSM [62] was first used to

identify clusters of Re in the data (0.7 nm with 0.7 nm bulk distance, N_{min} of 70). MSM was performed by a modified version of the posgen [63], code patch available as supplementary material. The modification produces line profiles scaled to the radius of gyration of each cluster, the same method as applied elsewhere [64]. If the cluster radius is r, then the total volume of the line profile is $5.2r^3$, where the length of the line profile parallel to the Z-direction is twice $1.3 \approx \sqrt{\frac{5}{3}}$ above and below the centre of mass of the cluster, and the line profile has a square cross section $\pm\frac{r}{2}$ in both X and Y. This volume is sectioned into 100 bins each with a Z-height of $\frac{5.2r}{100}$. The raw files, one per atom probe volume, are processed by the processLineProfiles.R script in R which aggregates all the composition and density line profile data together.

In total 102 clusters were detected and analysed using this method. For each line profile exported using the automated program, a peak detection method was applied in order to generate a measure of the peak concentration. The data was first rebinned into 20 groups with a width of 5 nm to improve counting statistics. The mean of each bin was calculated and the highest 85% of these bin means were selected and averaged, to capture the core of the cluster, to give the overall peak cluster concentration. The Os concentration was calculated using the same method for each of the Re bins included in this analysis.

The results from the line profile analysis along with the MSM results, details of which are available elsewhere, are summarised in figure 7. The results from the line profile analysis are plotted as circles, with the blue points representing data taken from the single crystal sample and red from the polycrystalline. As was observed using the MSM, the overall Re and Os concentration in the clusters is lower
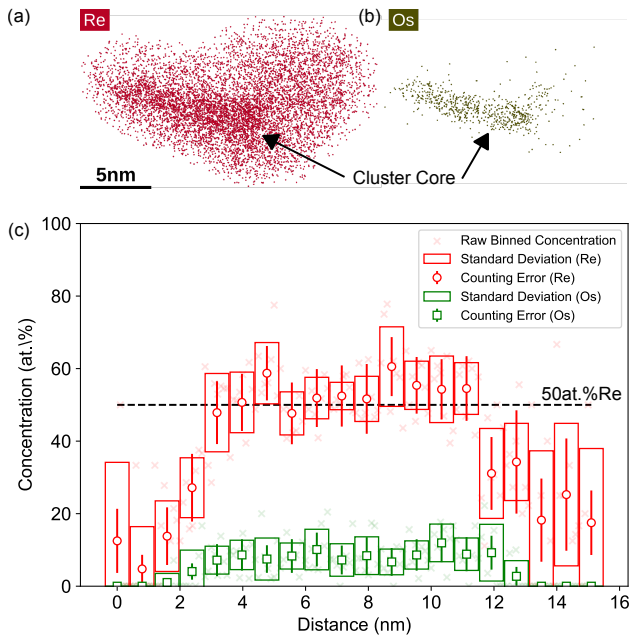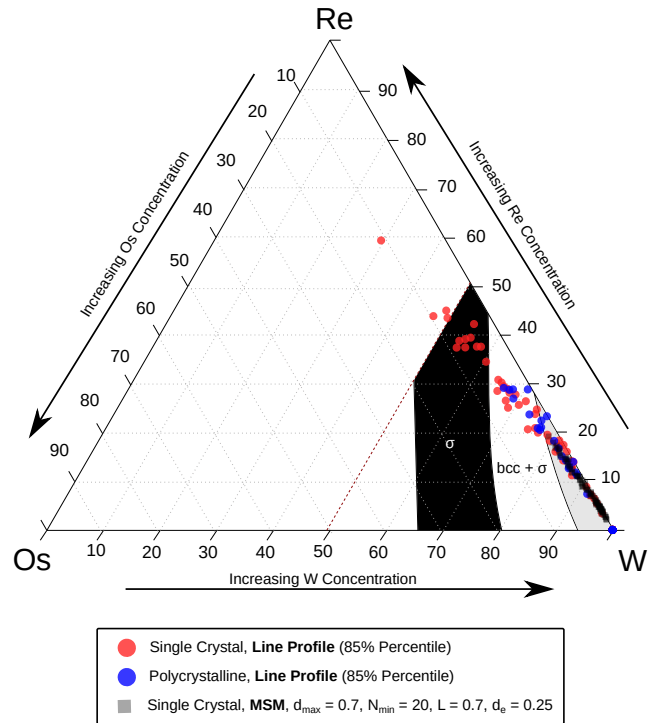
Figure 6: Shown in (a) and (b) are close-up images of the Re and Os atoms in the precipitate analysed in (c), with atoms plotted as spheres of radius 0.05nm. 100% of Re and Os atoms are shown respectively with all other atoms hidden for visual clarity. The boundary of the cluster was defined using a 5at.%Re isoconcentration surface. (c) Line profile taken through rod-shaped cluster in APT data, centred on a 25at.%Re isoconcentration surface. Cylindrical ROI of dimensions 1.64 nm radius, 1.5×10^1 nm long, binned into 152 bins along the z-direction of width 1×10^{-1} nm in IVAS, rebinned into 20 bins using Python. Errors plotted are both counting error from IVAS and the standard deviation on each bin.


Figure 7: Partial ternary phase diagram for W-Re-Os at 1873K isotherm, with the region in which σ phase formation is predicted highlighted in black. Overlaid are individual cluster compositions calculated from APT using various methods. The black points were obtained using conventional MSM, whereas the red and blue points were obtained using the line profile analysis method. The red points represent clusters in the single crystal sample, whereas the blue points are cluster from the polycrystalline material.

for the polycrystalline sample than the single crystal, as is shown by the average cluster composition given in table 3. The range of compositions from the line profile analysis is greater than for the MSM, with the maximum cluster composition being reported as 59at.%Re and 12at.%Os. The average cluster composition is fully within the bcc + σ phase region, with some clusters from the single crystal sample fully within the σ phase region.

3.4. Dislocation Decoration

In addition to precipitates and voids, APT analysis found evidence for the decoration of dislocations with both Re and Os transmutation products. Figure 8(a) shows one of the APT samples from figures 2 and 3 taken from the neutron irradiated, single crystal material, with the Re atoms plotted in red and the Os atoms plotted in green. There is a line of Os atoms within the highlighted square in figure 8(a), which is more clearly shown by the 0.5at.%Os isoconcentration surface in the higher magnification image shown in figure 8(b). Composition line profiles taken perpendicular and parallel to the dislocation are shown in figures 8(c) and (d) respectively. They highlight the decoration of the dislocation with both Re and Os. Figure 8(d), which is taken along a ROI orientated along the dislocation shows a Re concentration of

between 4-5at.%Re and 1-3at.%Os. This suggests that Os segregates most strongly to dislocations, as the concentration here has increased by over a factor of 10 with respect to the nominal concentration (0.08at.%) whereas Re has increased by around a factor of 3 from the nominal concentration (1.2at.%).

Figure 9(a) shows another APT data set from the single crystal neutron irradiated material, with the W atoms plotted in blue and the Re and Os atoms plotted separately as red and green spheres respectively. When compared to the clusters shown in figure 6 (a) and (b), the central Os rich region in figure 9(a) has a more diffuse interface, and is less dense in the core. Furthermore, the Os atoms in figure 9(a) are located around the periphery of the cluster, and as shown in figure 9(c), they form a ring shape around the edge of the Re. This indicates that this feature is a decorated dislocation loop. The Os ring is highlighted by the 0.5at.%Os isoconcentration surface in figure 9(b) in a similar way to the line dislocation observed in figure 8(b).

Figures 9(d) and (e) show line profiles taken through the centre of the loop and tangentially to the loop respectively. In both cases the ROIs were aligned manually with the plane of the Os atoms shown in figure 9(c). Figures 9(d) and (e)
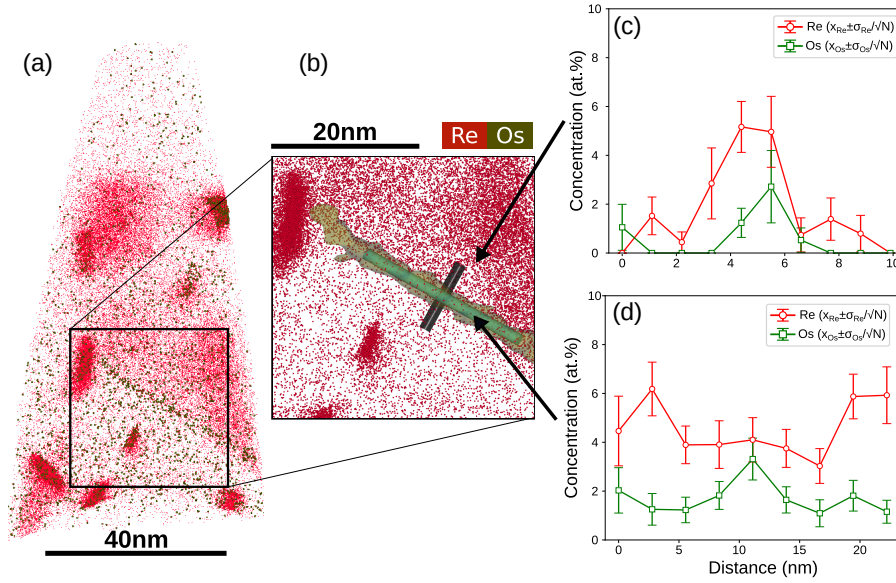
Figure 8: Segregation of Re and Os transmutation products to a line dislocation in W-1.4Re-0.1Os irradiated to 1.67dpa at 1173K, measured using APT. Shown in (a) is the full data set with Re atoms plotted in red and Os atoms in green, with (b) a higher magnification section of the sample with the line dislocation highlighted with a 0.5at.%Os isoconcentration surface. Plotted in (b) are the ROIs used to analyse the segregation of Re and Os to the dislocation. The plots shown in (c) and (d) show the line profile concentrations from the ROIs shown in (b) for the transverse and in-line directions respectively. In (c) and (d), the circular red points represent Re and the square green points represent Os. The error bar is given by the standard error, $\sigma_{\bar{x}}$ for each of the bins, calculated using $\sigma_{\bar{x}} = \sigma/\sqrt{N}$ where N is the number of points in each bin, and σ is the standard deviation of the bin concentration.

show that both Re and Os segregation to the loop has occurred. The Re segregation to the loop is stronger than was observed for the line dislocation in figure 8, with a central Re composition of between 10 and 12 at.%Re clear from figures 9(d) and (e). The two peaks in the Os concentration visible in figure 9(d) correspond to the two points at which the ROI crosses the Os isoconcentration surface shown in figure 9(b). There is clear segregation to the edge of the loop whereas in the centre where the concentration of Re is highest, there is no visible Os. The concentration of Os at the periphery of the loop is measured as between 1-4at.%Os, which is similar to the level observed for the line dislocation in figures 8(c) and (d).

3.5. Grain Boundary Decoration

A reconstruction of the targeted grain boundary APT sample, taken from the polycrystalline material, is shown in figure 10 (c) and (d). The grain boundary is located centrally within the reconstructed volume and is clearly highlighted by the red Re atoms and green Os atoms. Figure 10 (d) shows the reconstruction rotated by 90 degrees with respect to figure 10 (c). In the rotated view, there are individual lines of Os atoms. The structure within the grain boundary confirms that this is a low angle grain boundary, and that the lines visible in figure 10 (d) are individual dislocations. Figures 10 (a) and (b) show 1 dimensional line profiles taken perpendicular to, and parallel to, the grain boundary shown in figure 10 (c). The maximum concentration is between 5-6at.%Re and 0.5-1at.%Os. The variation due to individual dislocations within the grain boundary is shown clearly in

the parallel line profile in figure 10 (b).

4. Discussion

4.1. Transmutation Product Precipitation

The APT measurements of bulk sample compositions summarised in table 1, confirm the findings or previous studies with more limited data. The polycrystalline sample had a lower overall Re concentration than the single crystal sample, but this is likely due to the APT samples being taken from near to an adjacent grain boundary. Previous studies have found strong Re decoration of grain boundaries. More detailed measurements of the isotopic concentration in the samples, summarised in table 2 showed good agreement with the FISPACT-II simulations. This demonstrates clearly that FISPACT-II simulations are a reliable means of assessing neutron radiation induced changes to sample composition in W materials, provided that an accurate description of the neutron energy spectrum is available.

As has been reported in previous preliminary analyses of the samples irradiated at HFR, we observe clear evidence for the strong segregation of both Re and Os. In small scale APT studies of this material by Lloyd et. al [29], precipitates were observed with a Re and Os core shell structure. As highlighted by figures 2-5, here this finding is confirmed with a more extensive analysis. The majority of the clusters analysed contained Os, with only a small percentage containing only Re. A subset of the precipitates exhibit a rod shaped morphology, with some of the clusters containing
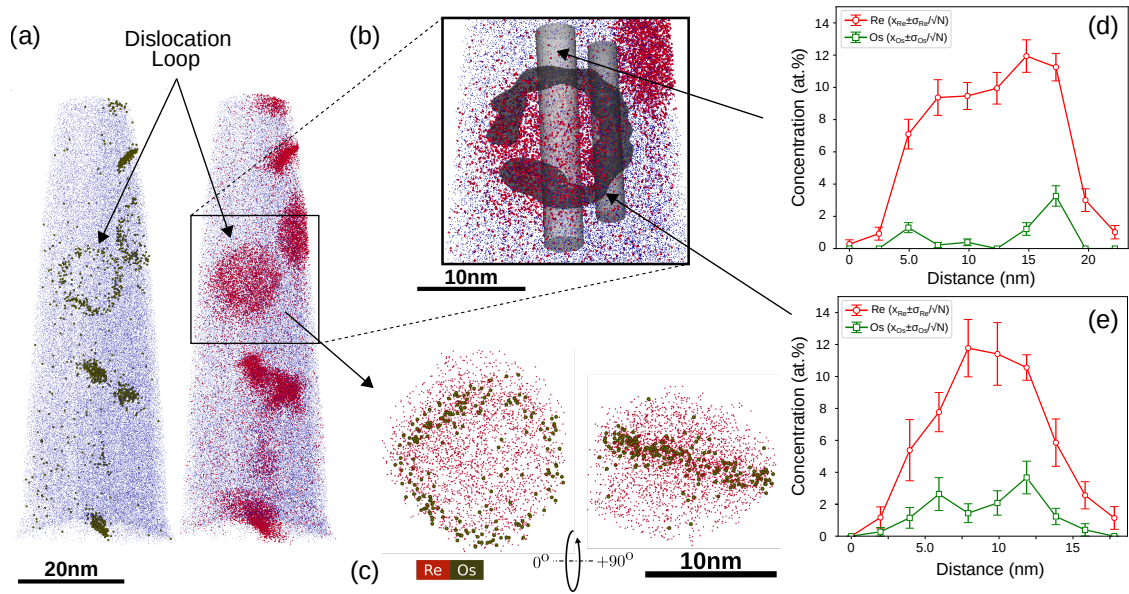
Figure 9: Segregation of Re and Os transmutation products to a dislocation loop in W-1.4Re-0.1Os irradiated to 1.67dpa at 1173K, measured using APT. Shown in (a) is the full reconstructed volume showing 8% of W atoms for visual clarity and Os atoms as green spheres 0.2 nm in diameter, and Re atoms as red spheres of 0.1 nm diameter in order to highlight the respective positions of these atoms. Shown in (b) and (c) are higher magnification views of the loop shown in (a), with the position of the Os atoms highlighted with a 0.5at.%Os isoconcentration surface in (b) with two cylindrical ROIs defined across the middle of the loop and on the periphery. Shown in (c) is a volume extracted with a Re isoconcentration surface at two different orientations which are rotated 90° with respect to one another, with all W atoms removed. The Re atoms are plotted as small red points and the Os atoms are plotted as spheres of 0.1 nm diameter in order to highlight there position within the volume. Plotted in figures (d) and (e) are the line profile analyses from the central and peripheral ROIs respectively, with Re plotted as red circles and Os plotted as green squares. The error bar is given by the standard error, $\sigma_{\bar{x}}$ for each of the bins, calculated using $\sigma_{\bar{x}} = \sigma/\sqrt{N}$ where N is the number of points in each bin, and σ is the standard deviation of the bin concentration.

a rod shaped core. The impact of voids on the APT data was unclear, but the combination of complementary STEM and atomic density measurements in the reconstruction of the APT data suggest that voids may be present in the analysed volume of material, and that these voids are decorated with Re and Os [29]. Correlative microscopy with APT and TEM is required to fully understand the impact of voids on these materials.

Analysis of the cluster compositions using a MSM shows that the precipitates are similar to those observed in other APT analyses of low transmutation rate neutron irradiation experiments, as is reported elsewhere [44]. Analysis shows an average cluster composition of 8.5at.%Re and 0.6at.%Os, which is well within the solid solution bcc region of the ternary W-Re-Os phase diagram. The cluster compositions are highly variable, as reflected in the standard deviation for the Re and Os cluster composition, which is 3.4 and 0.6 respectively. A similar range of values was observed by Edmmondson et. al in neutron irradiated tungsten from the HFIR [37].

Closer examination of the precipitates showed that some incorporated a denser Re and Os rich region in the centre of a more diffuse Re cloud, as shown in figure 6 (a) and (b). Line profile analysis of the central region of the precipitate shown in figure 6 (a) and (b), plotted in figure 6 (c), shows that the central region of this precipitate has a composition

consistent with σ phase, something that has not been previously reported for this sample.

Statistical analysis was performed on the full set of data shown in figures 2-5 using a line profile and concentration peak fitting method. The results are summarised in figure 7, along with the MSM data reported elsewhere for this sample. Comparing the line profile data with that from the MSM, there is clearly a higher maximum reported concentration, with one cluster from the single crystal sample having as high as 59at.%Re and 11at.%Os. As summarised in table 3, the average cluster composition reported from the line profile method is considerably higher than with the MSM, at approximately 25at.%Re and 3.4at.%Os. The data is also more variable, with a considerably higher standard deviation calculated for the line profile method. This is reflected in the data plotted in figure 7, where some of the clusters are within the solid solution bcc region of the phase diagram, and others extend well into the σ phase region and beyond. The structure of the clusters, shown in figure 6, suggest that the MSM of this material gives an average cluster composition that accounts for both the Re and Os rich core and the diffuse Re cloud around this.

These results highlight that the precipitates are not homogeneous regions rich in Re and Os, but rather have an outer region of Re with a central dense, typically rod shaped core, which is highly concentrated in Re and Os. The re-
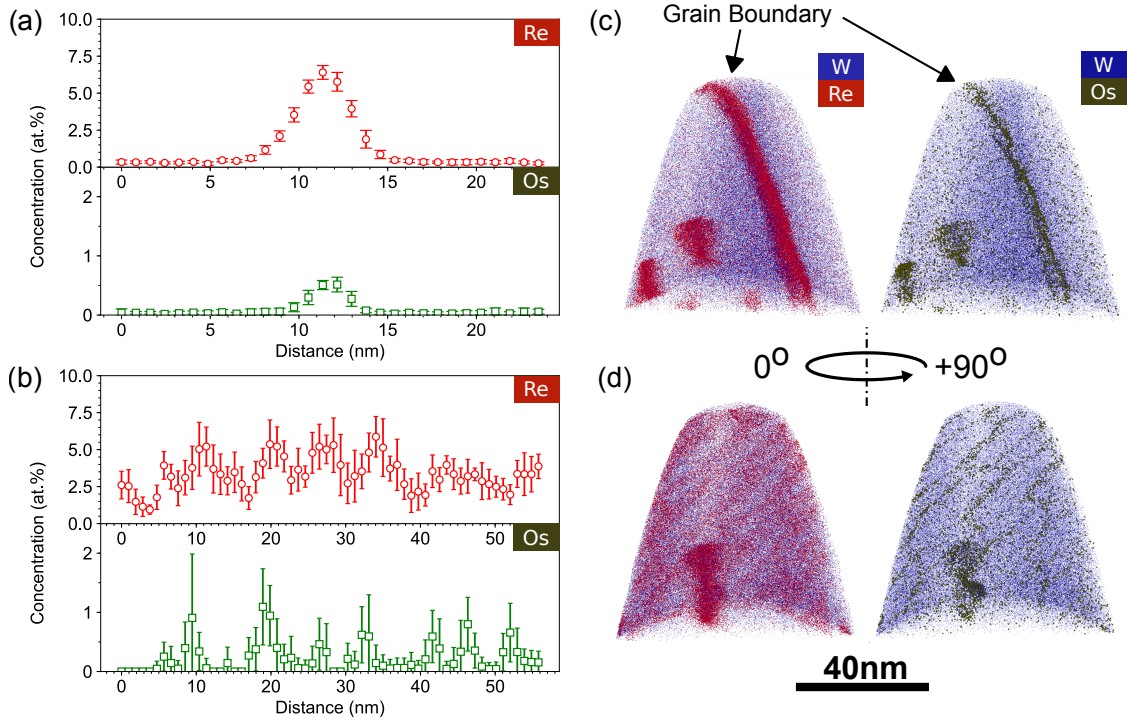
Figure 10: Decoration of a grain boundary in the polycrystalline neutron irradiated sample, with Re and Os transmutation products. (a) and (b) show line concentration line profiles taken across the grain boundary shown in figures (c), perpendicular to and parallel to the boundary respectively (note that the x-axis on (a) and (b) are plotted using different scales). (d) shows the reconstruction in (c), but rotated by 90 degrees. The data was extracted from IVAS in bins of width 0.1nm, and then re-binned into (a) 30 and (b) 60 concentration bins. The error bar is given by the standard error, $\sigma_{\bar{x}}$ for each of the bins, calculated using $\sigma_{\bar{x}} = \sigma/\sqrt{N}$ where N is the number of points in each bin, and σ is the standard deviation of the bin concentration.

sults suggest that in the centre of the precipitates either the formation of σ phase or the onset of σ phase formation has occurred. However, prior diffraction pattern analysis of this material did not measure a signal from σ phase, most likely due to the small size of the region in which σ phase formation has occurred.

4.2. DFT Interpretation of Dislocation Decoration

Decoration of dislocations, and loops was observed in the single crystal sample, and contained within the sub-grain boundary in the polycrystalline material. The decoration of dislocations with Os appeared to be strongest with Os typically located at the edge of the dislocation or loop. This agrees with early APT studies of W-Os in which Os was found to decorate dislocations in W [43]. The Re appears to also segregate to the dislocations but is more weakly bound than the Os. This highlights that dislocations will act as potential nucleation sites for precipitates, but that stronger precipitates formation was observed here at sites not associated with dislocations.

Figure 11 shows the binding energy of Ta, Re and Os with a 37 SIA < 111 > loop in bcc-W versus the distance to the loop center. For all solutes, the interaction inside the loop is either small (below 0.5 eV) or repulsive in the case of Ta. For Os and Re, the interaction becomes meaningful and in fact quite high for Os (1.3 eV) at the loop periphery, i.e. on the last shell of the loop, and more precisely at the corner
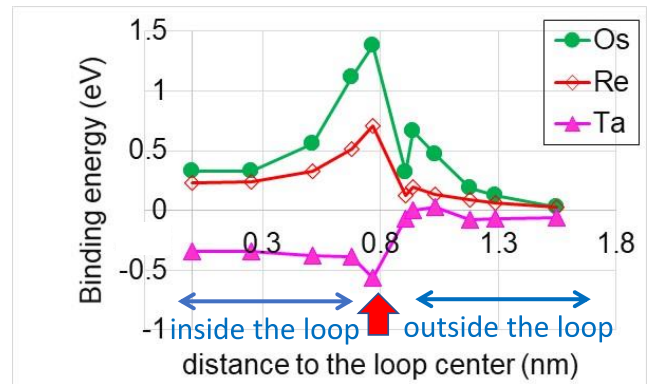
Figure 11: Plot of the binding energy calculated using DFT with elastic correction between Re, Os and Ta solute atoms within a 37 SIA < 111 > loop in bcc-W, versus distance to the loop center. The data have been obtained using 2 x 2 x 2 kpoints. The red arrow indicates the loop periphery. Within our reference, a positive binding energy indicates an attractive interaction

of the last shell. These are sites which are in compression and the local volume available for the solute is smaller than in the bulk. A similar behaviour had been observed for solutes such as P, Mn, Ni and Si in Fe [65]. Outside the loop, the interaction is attractive but it quickly becomes negligible: the range of the interaction between the solutes and the
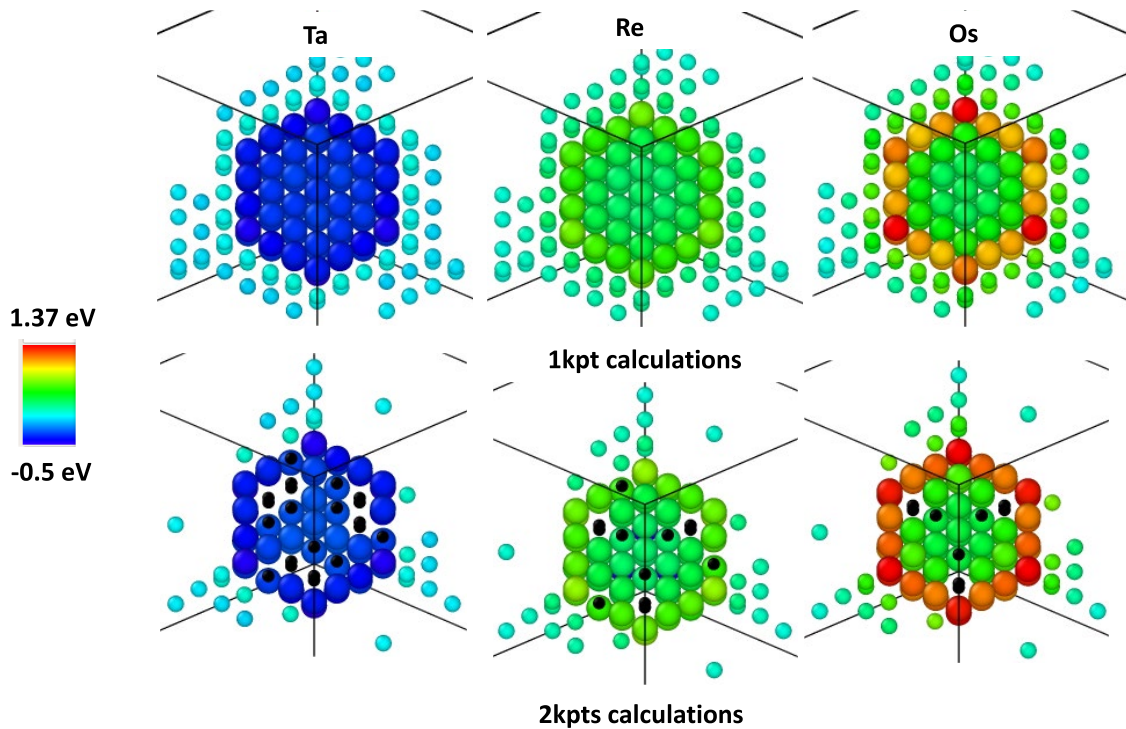
Figure 12: Binding energy between single Ta, Re or Os solute atoms, with a SIA < 111 > loop in bcc-W, in various positions. The positions are coloured by their respective binding energy, where a negative binding energy indicates a repulsive interaction. The small black points for the 2kpts figure represent positions for which the binding energy was not calculated. The atoms of the loops are represented with larger radius.

loop is very short.

For Ta, the interaction remains negligible whatever its position (inside or outside the loop). The trends in the binding energies follow nicely the periodic table: for these three elements, the smaller the atom, the larger the interaction with the loop. Ta atoms being larger than W atoms, are not attracted by the loop, whereas Re and Os which are smaller atoms than W atoms are attracted by the loop. The contribution of the size effect to the interaction is thus non negligible in that case. Figure 12 shows the binding energy of a single solute atom with the solute for different position of the solute. As already exemplified in Figure 11, one sees that the interaction is the strongest for the solute at the periphery of the loop and more precisely at the corner of the loop where the strain is the highest. Os is the solute for which the interaction is the highest. Note also that as mentioned in the methodology section, the binding energies are very similar whether calculated with 1 or 2 kpts (See more detailed analysis of binding energy using a different scale for each solute in Appendix.)

The APT results are fully in agreement with the DFT results which indicate that Os bind the strongest with the loop and that Ta does not bind at all. We propose that the reason Os is mostly seen at the periphery of the loops is because it is the solute species with the strongest interaction with the loop, and because the most stable configuration for solute atoms that bind with the loop is at the periphery. Os atoms therefore occupy these sites at the perihpery of the loop pref-

erentially to Re, which binds less strongly. Re atoms are present in larger amounts in the sample and thus are found at the periphery of the loop as well as on other binding sites. Re atoms are therefore found inside the loop, even if there it is less favourable. We checked whether introducing another Re or Os atom in the vicinity of Re or Os atom in the loop for various positions would change the binding energy of the solute with the loop and it just decreases it moderately. Thus within the present study, it seems to be no real co-segregation effect between the two solutes in the loop

It is worth emphasising that the systematic trend of increasing binding energy for the three solute elements interacting with dislocation loops shown in Figs. 11 and 12 is very consistent with those obtained from both DFT and Monte-Carlo simulations of voids decorated by Ta, Re and Os [66, 67]. The presence of both rhenium and osmium inside voids induced by neutron irradiation [29, 49] is seen to be sensitive to the concentration of transmutation elements and the correlation between their positions can be interpret in term of short-range order effect between Re and Os [66].

5. Conclusion

In this study, an APT characterisation of high temperature, neutron irradiated W is presented, which has particular relevance to the evolution of W reactor components in a fusion power station. Based on the analysis presented in this study, the following conclusions can be made:
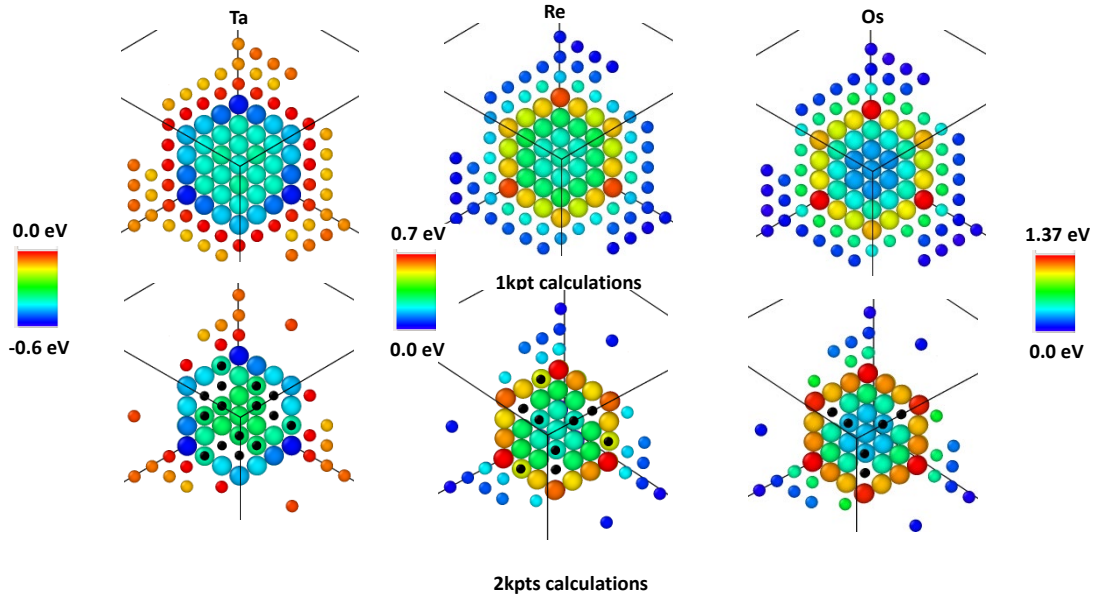
Figure 13: Binding energy between single Ta, Re or Os solute atoms, with a SIA < 111 > loop in bcc-W, in various positions, each coloured using a separate scale. The positions are coloured by their respective binding energy, where a negative binding energy indicates a repulsive interaction. The small black points for the 2kpts figure represent positions for which the binding energy was not calculated. The atoms of the loops are represented with larger radius.

1. FISPACT-II simulations were generally in good agreement with the measured abundances, both in terms of bulk sample composition and with respect to individual W, Re, Os and Ta isotopes produced via transmutation. This demonstrates clearly that this is a reliable and effective means of assessing post-irradiation sample composition in W, provided an accurate description of the neutron energy spectrum is available.

2. Production of Re and Os in a low transmutation rate irradiation led to the formation of Re and Os rich precipitates. Os segregation was very strong, despite the lower nominal concentration.

3. The precipitates formed under neutron irradiation consisted of a central Re and Os rich core, with a composition consistent with that of the σ phase observed elsewhere, surrounded by a more diffuse cloud of Re atoms.

4. Automated line profile analysis found that on average the clusters had a composition of 24.6at.%Re and 0.6at.%Os, but that the individual cluster composition varied significantly about this mean value.

5. Dislocation loops in W were observed to be decorated with Os, and a diffuse cloud of Re. The Os formed a ring around the edge of the loop, with a maximum concentration of ≈2at.%Os. A systematic DFT investigation of interaction between solutes and the SIA < 111 > dislocation loop in W demonstrates that Os had the strongest binding energy with the loop in agreement with the present experimental findings

6. Low angle grain boundaries were shown to be decorated with both Re and Os transmutation products. Re

was present in a higher concentration but the relative increase in the concentration with respect to the bulk composition was highest for Os. A maximum concentration at the grain boundary of between 5-6at.%Re and 0.5-1at.%Os was observed.

These observations have important ramifications for the development of W fusion reactor components. In particular, the finding that low nominal Os concentrations can significantly alter the precipitate structure highlights the importance of understanding the early (low transmutant concentration) stages of transmutation in a reactor. It also clearly demonstrates the need for more representative samples, with fusion relevant transmutation rates, to properly understand the competing and synergistic roles of Os and Re in precipitate formation.

A. Detailed analysis of DFT binding energy for interaction between loops and each of solute elements

Figure 13 shows the binding energy between a single Ta, Re or Os solute atom with the 37 SIA < 111 > loop in bcc-W, shown in figure 12. In figure 13, the colour bar for each solute element is plotted separately, whereas in figure 12 all are plotted with the same scale. Figure 13 shows that for Re, the highest binding energy is at the periphery of the loop, as is the case for Os, but that the Os binding is far stronger than for Re.

Acknowledgements

References

[1] Nuclear Energy Agency. *Java-based Nuclear Data Information System*, 17 February 2019 (accessed 24 August, 2020). https://www.oecd-nea.org/janis/.

[2] D.A. Brown, M.B. Chadwick, R. Capote, A.C. Kahler, A. Trkov, M.W. Herman, A.A. Sonzogni, Y. Danon, A.D. Carlson, M. Dunn, D.L. Smith, G.M. Hale, G. Arbanas, R. Arcilla, C.R. Bates, B. Beck, B. Becker, F. Brown, R.J. Casperson, J. Conlin, D.E. Cullen, M.-A. Descalle, R. Firestone, T. Gaines, K.H. Guber, A.I. Hawari, J. Holmes, T.D. Johnson, T. Kawano, B.C. Kiedrowski, A.J. Koning, S. Kopecky, L. Leal, J.P. Lestone, C. Lubitz, J.I. Màrquez Damiàn, C.M. Mattoon, E.A. McCutchan, S. Mughabghab, P. Navratil, D. Neudecker, G.P.A. Nobre, G. Noguere, M. Paris, M.T. Pigni, A.J. Plompen, B. Pritychenko, V.G. Pronyaev, D. Roubtsov, D. Rochman, P. Romano, P. Schillebeeckx, S. Simakov, M. Sin, I. Sirakov, B. Sleaford, V. Sobes, E.S. Soukhovitskii, I. Stetcu, P. Talou, I. Thompson, S. van der Marck, L. Welser-Sherrill, D. Wiarda, M. White, J.L. Wormald, R.Q. Wright, M. Zerkle, G. Ảịerovnik, and Y. Zhu. Endf/b-viii.0: The 8th major release of the nuclear reaction data library with cielo-project cross sections, new standards and thermal scattering data. *Nuclear Data Sheets*, 148:1 – 142, 2018. Special Issue on Nuclear Reaction Data.

[3] Mark R. Gilbert and Jean-Christophe Sublet. *Handbook of activation, transmutation, and radiation damage properties of the elements simulated using FISPACT-II and TENDL-2015; Magnetic Fusion Plants*. UKAEA.

[4] MR Gilbert and J-Ch Sublet. Neutron-induced transmutation effects in w and w-alloys in a fusion environment. *Nuclear Fusion*, 51(4):043005, 2011.

[5] M. R. Gilbert, T. Eade, T. Rey, R. Vale, C. Bachmann, U. Fischer, and N. P. Taylor. Waste implications from minor impurities in european DEMO materials. *Nucl. Fus.*, 59:076015, 2019. https://doi.org/10.1088/1741-4326/ab154e.

[6] David R Lide. *CRC Handbook of Chemistry and Physics*, volume 85. CRC press, 2004.

[7] T Tanabe, C Eamchotchawalit, C Busabok, S Taweethavorn, M Fujitsuka, and Tatsuo Shikama. Temperature dependence of thermal conductivity in w and w–re alloys from 300 to 1000 k. *Materials Letters*, 57(19):2950–2953, 2003.

[8] MJ Baldwin and RP Doerner. Helium induced nanoscopic morphology on tungsten under fusion relevant plasma conditions. *Nuclear Fusion*, 48(3):035001, 2008.

[9] RG Abernethy, JSK-L Gibson, A Giannattasio, JD Murphy, O Wouters, S Bradnam, LW Packer, MR Gilbert, M Klimenkov, M Rieth, et al. Effects of neutron irradiation on the brittle to ductile transition in single crystal tungsten. *Journal of Nuclear Materials*, 527:151799, 2019.

[10] Peter L Raffo. Yielding and fracture in tungsten and tungsten-rhenium alloys. *Journal of the Less Common Metals*, 17(2):133–149, 1969.

[11] Brady G Butler, James D Paramore, Jonathan P Ligda, Chai Ren, Z Zak Fang, Scott C Middlemas, and Kevin J Hemker. Mechanisms of deformation and ductility in tungsten–a review. *International Journal of Refractory Metals and Hard Materials*, 75:248–261, 2018.

[12] A. Gilbert. A Fractographic Study of Tungsten and Dilute Tungsten-Rhenium Alloys. *Journal of the Less Common Metals*, 10(5):328–343, 1966.

[13] Bernd Gludovatz, Stefan Wurster, Tobias Weingärtner, Andreas Hoffmann, and Reinhard Pippan. Influence of Impurities on the Fracture Behaviour of Tungsten. *Philosophical Magazine*, 91(22):3006–3020, 2011.

[14] E. Gaganidze, A. Chauhan, H.-C. Schneider, D. Terentyev, G. Borghmans, and J. Aktaa. Fracture-mechanical properties of neutron irradiated iter specification tungsten. *Journal of Nuclear Materials*, 547:152761, 2021.

[15] DEJ Armstrong, PD Edmondson, and SG Roberts. Effects of sequential tungsten and helium ion implantation on nano-indentation hardness of tungsten. *Applied Physics Letters*, 102(25):251901, 2013.

[16] Alan Xu, Christian Beck, David EJ Armstrong, Krishna Rajan, George DW Smith, Paul AJ Bagot, and Steve G Roberts. Ion-irradiation-induced clustering in w–re and w–re–os alloys: A comparative study using atom probe tomography and nanoindentation measurements. *Acta Materialia*, 87:121–127, 2015.

[17] Alan Xu, David EJ Armstrong, Christian Beck, Michael P Moody, George DW Smith, Paul AJ Bagot, and Steve G Roberts. Ion-irradiation induced clustering in w-re-ta, w-re and w-ta alloys: An atom probe tomography and nanoindentation study. *Acta Materialia*, 124:71–78, 2017.

[18] T Hwang, M Fukuda, S Nogami, A Hasegawa, H Usami, K Yabuuchi, K Ozawa, and H Tanigawa. Effect of self-ion irradiation on hardening and microstructure of tungsten. *Nuclear Materials and Energy*, 9:430–435, 2016.

[19] ZX Zhang, DS Chen, WT Han, and A Kimura. Irradiation hardening in pure tungsten before and after recrystallization. *Fusion Engineering and Design*, 98:2103–2107, 2015.

[20] DEJ Armstrong, AJ Wilkinson, and SG Roberts. Mechanical properties of ion-implanted tungsten–5 wt% tantalum. *Physica Scripta*, 2011(T145):014076, 2011.

[21] Xunxiang Hu, Takaaki Koyanagi, Makoto Fukuda, Yutai Katoh, Lance L. Snead, and Brian D. Wirth. Defect evolution in single crystalline tungsten following low temperature and low dose neutron irradiation. *Journal of Nuclear Materials*, 470(December 2015):278–289, 2016.

[22] Akira Hasegawa, Makoto Fukuda, Kiyohiro Yabuuchi, and Shuhei Nogami. Neutron irradiation effects on the microstructural develop-

ment of tungsten and tungsten alloys. *Journal of Nuclear Materials*, 471:175–183, 2016.

[23] Y Katoh, LL Snead, Lauren M Garrison, Xunxiang Hu, Takaaki Koyanagi, Chad M Parish, PD Edmondson, Makoto Fukuda, Taehyun Hwang, T Tanaka, et al. Response of unalloyed tungsten to mixed spectrum neutrons. *Journal of Nuclear Materials*, 520:193–207, 2019.

[24] JC He, GY Tang, A Hasegawa, and K Abe. Microstructural development and irradiation hardening of w and w–(3–26) wt% re alloys after high-temperature neutron irradiation to 0.15 dpa. *Nuclear fusion*, 46(11):877, 2006.

[25] Chao Yin, Dmitry Terentyev, Andrii Dubinko, Tao Zhang, Marius Wirtz, Steffen Antusch, Roumen H Petrov, and Thomas Pardoen. Impact of neutron irradiation on hardening of baseline and advanced tungsten grades and its link to initial microstructure. *Nuclear Fusion*, 61(6):066012, 2021.

[26] Felix Hofmann, Daniel R Mason, Jeffrey K Eliason, Alexei A Maznev, Keith A Nelson, and Sergei L Dudarev. Non-contact measurement of thermal diffusivity in ion-implanted nuclear materials. *Scientific reports*, 5:16042, 2015.

[27] Abdallah Reza, Hongbing Yu, Kenichiro Mizohata, and Felix Hofmann. Thermal diffusivity degradation and point defect density in self-ion implanted tungsten. *Acta Materialia*, 2020.

[28] MR Gilbert, J-Ch Sublet, and SL Dudarev. Spatial heterogeneity of tungsten transmutation in a fusion device. *Nuclear Fusion*, 57(4):044002, 2017.

[29] Matthew J Lloyd, Robert G Abernethy, Mark R Gilbert, Ian Griffiths, Paul AJ Bagot, Duc Nguyen-Manh, Michael P Moody, and David EJ Armstrong. Decoration of voids with rhenium and osmium transmutation products in neutron irradiated single crystal tungsten. *Scripta Materialia*, 173:96–100, 2019.

[30] MR Gilbert, SL Dudarev, D Nguyen-Manh, S Zheng, LW Packer, and J-Ch Sublet. Neutron-induced dpa, transmutations, gas production, and helium embrittlement of fusion materials. *Journal of Nuclear Materials*, 442(1-3):S755–S760, 2013.

[31] MR Gilbert, T Eade, C Bachmann, U Fischer, and NP Taylor. Activation, decay heat, and waste classification studies of the european demo concept. *Nuclear Fusion*, 57(4):046015, 2017.

[32] William D Klopp. *Review of ductilizing of group VIA elements by rhenium and other solutes*, volume 4955. National Aeronautics and Space Administration, 1968.

[33] Chai Ren, Z.Zak Fang, Mark Koopman, Brady Butler, James Paramore, and Scott Middlemas. Methods for improving ductility of tungsten - a review. *International Journal of Refractory Metals and Hard Materials*, 75:170 – 183, 2018.

[34] Yong-Jie Hu, Michael R. Fellinger, Brady G. Butler, Yi Wang, Kristopher A. Darling, Laszlo J. Kecskes, Dallas R. Trinkle, and Zi-Kui Liu. Solute-induced solid-solution softening and hardening in bcc tungsten. *Acta Materialia*, 141:304 – 316, 2017.

[35] William D. Klopp. A review of chromium, molybdenum, and tungsten alloys. *Journal of the Less Common Metals*, 42(3):261 – 278, 1975.

[36] RK Williams, FW Wiffen, J Bentley, and JO Stiegler. Irradiation induced precipitation in tungsten based, w-re alloys. *Metallurgical Transactions A*, 14(3):655–666, 1983.

[37] Philip D Edmondson, Baptiste Gault, and Mark R Gilbert. An atom probe tomography and inventory calculation examination of second phase precipitates in neutron irradiated single crystal tungsten. *Nuclear Fusion*, 60(12):126013, 2020.

[38] Rempe, J. and Knudson, D. and Condie, K. and Cole, J. Long Duration Performance of High Temperature Irradiation Resistant Thermocouples. volume 4, 05 2007.

[39] P. Villars, A. Prince, and H. Okamoto. *Handbook of Ternary Alloy Phase Diagrams: Mg-Ni-P to Y-Zn-Zr*. ASM International, Materials Park, OH, USA, 2006.

[40] Michael Dürrschnabel, Michael Klimenkov, Ute Jäntsch, Michael Rieth, Hans-Christian Schneider, and Dmitry Terentyev. New microstructural insights into neutron-irradiated tungsten. 2020.

[41] C.-H. Huang, L. Gharaee, Y. Zhao, P. Erhart, and J. Marian. Mechanism of Nucleation and Incipient Growth of Re Clusters in Irradiated W-Re Alloys from Kinetic Monte Carlo Simulations. *Physical Review B*, 96(9):094108, 2017.

[42] M. J. Lloyd, R. G. Abernethy, D. E. J. Armstrong, P. A. J. Bagot, M. P. Moody, E. Martinez, and D. Nguyen-Manh. Radiation-Induced Segregation in W-Re: from Kinetic Monte Carlo Simulations to Atom Probe Tomography Experiments. *The European Physical Journal B*, 92(10):241, 2019.

[43] HC Eaton and Hans Nordén. The segregation of osmium to grain boundary dislocations in tungsten. *Scripta metallurgica*, 17(8):1043–1046, 1983.

[44] M. Lloyd. *A Thesis Submitted for the Degree of Doctor of Philosophy: Radiation Damage and Transmutation in Tungsten*. PhD thesis, Department of Materials, University of Oxford, 2021.

[45] M. J. Lloyd, B. Jim, J. Haley, R. Abernethy, E. Martinez, O. El-Atwani, D. Nguyen-Manh, M. P. Moody, P. A. J. Bagot, and D. E. J. Armstrong. A Comparison between Ion and Neutron Irradiated W for Fusion Applications. *Acta Materialia*, To be submitted, 2021.

[46] Robert Abernethy. A thesis submitted for the degree of doctor of philosophy: Comparison of ion and neutron irradiation of tungsten for fusion applications. 2019.

[47] J-Ch Sublet, JW Eastwood, JG Morgan, MR Gilbert, M Fleming, and W Arter. Fispact-ii: an advanced simulation system for activation, transmutation and material modelling. *Nuclear Data Sheets*, 139:77–137, 2017.

[48] A. J. Koning, D. Rochman, et al. TENDL-2015. Release Date: January 18, 2016. Available from https://tendl.web.psi.ch/tendl_2015/tendl2015.html.

[49] M Klimenkov, U Jäntsch, M Rieth, HC Schneider, DEJ Armstrong, J Gibson, and SG Roberts. Effect of neutron irradiation on the microstructure of tungsten. *Nuclear Materials and Energy*, 9:480–483, 2016.

[50] *AtomProbeLab: Matlab-based analysis of Atom Probe Data*, 30/06/2016 (accessed 27 August, 2020). https://sourceforge.net/projects/atomprobelab/.

[51] G. Kresse and J. Furthmüller. Efficient iterative schemes for ab initio total-energy calculations using a plane-wave basis set. *Phys. Rev. B*, 54:11169–11186, Oct 1996.

[52] G. Kresse and J. Furthmüller. Efficiency of ab-initio total energy calculations for metals and semiconductors using a plane-wave basis set. *Comput. Mater. Sci.*, 6(1):15–50, 1996.

[53] John P. Perdew, Kieron Burke, and Matthias Ernzerhof. Generalized gradient approximation made simple. *Phys. Rev. Lett.*, 77:3865–3868, Oct 1996.

[54] Céline Varvenne, Fabien Bruneval, Mihai-Cosmin Marinica, and Emmanuel Clouet. Point defect modeling in materials: Coupling ab initio and elasticity approaches. *Phys. Rev. B*, 88:134102, Oct 2013.

[55] Xunxiang Hu, Chad M Parish, Kun Wang, Takaaki Koyanagi, Benjamin P Eftink, and Yutai Katoh. Transmutation-induced precipitation in tungsten irradiated with a mixed energy neutron spectrum. *Acta Materialia*, 165:51–61, 2019.

[56] Charles Fletcher, Michael P Moody, and Daniel Haley. Towards model-driven reconstruction in atom probe tomography. *Journal of Physics D: Applied Physics*, 53(47):475303, sep 2020.

[57] Xing Wang, Constantinos Hatzoglou, Brian Sneed, Zhe Fan, Wei Guo, Ke Jin, Di Chen, Hongbin Bei, Yongqiang Wang, William J Weber, et al. Interpreting nanovoids in atom probe tomography data for accurate local compositional measurements. *Nature communications*, 11(1):1–11, 2020.

[58] Baptiste Gault, Michael P Moody, Julie M Cairney, and Simon P Ringer. *Atom probe microscopy*, volume 160. Springer Science & Business Media, 2012.

[59] *APTTools: A collection of utilities for atom probe tomography analysis*, 30-06-2020 (accessed March, 2020). https://sourceforge.net/projects/posgen.apttools.p/.

[60] Taehyun Hwang, Akira Hasegawa, Keiko Tomura, Naoki Ebisawa, Takeshi Toyama, Yasuyoshi Nagai, Makoto Fukuda, Takeshi Miyazawa, Teruya Tanaka, and Shuhei Nogami. Effect of neutron

irradiation on rhenium cluster formation in tungsten and tungsten-rhenium alloys. *Journal of Nuclear Materials*, 507:78–86, 2018.

[61] Makoto Fukuda, Takashi Tanno, Shuhei Nogami, and Akira Hasegawa. Effects of re content and fabrication process on microstructural changes and hardening in neutron irradiated tungsten. *Materials Transactions*, 53(12):2145–2150, 2012.

[62] JM Hyde and CA English. Symposium r: microstructural processes in irradiated materials. In *Mater. Res. Soc. Symp. Proc*, volume 650, page R6, 2000.

[63] Daniel Haley. Posgen. `http://apttools.sourceforge.net`, 2007–2020.

[64] A.J. London, S. Lozano-Perez, M.P. Moody, S. Amirthapandian, B.K. Panigrahi, C.S. Sundar, and C.R.M. Grovenor. Quantification of oxide particle composition in model oxide dispersion strengthened steel alloys. *Ultramicroscopy*, 159:360–367, December 2015.

[65] C. Domain and C.S. Becquart. Solute - <111> interstitial loop interaction in α-fe: A dft study. *Journal of Nuclear Materials*, 499:582–594, 2018.

[66] D. Nguyen-Manh, J. S. Wróbel, M. Klimenkov, M. J. Lloyd, L. Messina, and S.L. Dudarev. First-Principles Model for Voids Decorated by Transmutation Solutes: Short-Range Order Effects and Application to Neutron Irradiated Tungsten. *Phys. Rev. Mater.: Accepted for publication*, http://arxiv.org/abs/2102.01614, 2021.

[67] M. J. Lloyd, E. Martinez, L. Messina, and D. Nguyen-Manh. Development of a Solute and Defect Concentration Dependant Ising Model for the Study of Transmutation Induced Segregation in Neutron Irradiated W-(Re,Os) Systems. *Journal of Physics: Condensed Matter*, Under Review, 2021.